IOP Publishing and International Atomic Energy Agency Nuclear Fusion
Nucl. Fusion **49** (2009) 125009 (8pp) doi:10.1088/0029-5515/49/12/125009

The importance of parallel nonlinearity in the self-interaction of geodesic acoustic mode

H.S. Zhang[1,2], **Z. Qiu**[2,3], **L. Chen**[2,4] **and Z. Lin**[2,a]

[1] State Key Laboratory of Nuclear Physics and Technology, School of Physics, Peking University, Beijing 100871, People's Republic of China
[2] Department of Physics and Astronomy, University of California, Irvine, CA 92697, USA
[3] Department of Modern Physics, University of Science and Technology of China, Hefei 230026, People's Republic of China
[4] Institute for Fusion Theory and Simulation, Zhejiang University, Hangzhou 310027, People's Republic of China

E-mail: zhihongl@uci.edu

Received 23 March 2009, accepted for publication 21 October 2009
Published 10 November 2009
Online at stacks.iop.org/NF/49/125009

Abstract
Gyrokinetic theory and simulation find that the nonlinear self-interactions of the long wavelength geodesic acoustic mode (GAM) in toroidal plasmas cannot efficiently generate the second harmonic due to a cancellation between the perpendicular convective nonlinearity and the parallel nonlinearity, which is neglected in most of gyrokinetic theory and simulation. Other mechanisms beyond conventional GAM theory are required to explain recent experimental observations of the excitation of the GAM second harmonic.

PACS numbers: 52.30.Gz, 52.35.−g, 52.35.Fp, 52.35.Mw, 52.35.Qz

1. Introduction

Geodesic acoustic mode (GAM) [1] is an electrostatic oscillation in toroidal plasmas with a potential perturbation dominated by an $n = m = 0$ component (n and m are the toroidal and poloidal mode numbers, respectively) and a density perturbation dominated by an $n = 0, m = 1$ component. GAM has a real frequency $\omega_{\rm GAM}$ on the order of $c_{\rm s}/R$ ($c_{\rm s}$ is the ion sound speed and R is the major radius) and a linear damping rate γ which becomes smaller with a higher safety factor q and a lower collisionality [2, 3]. GAM has been widely observed [4] in tokamaks in the search for its counterpart, the zero-frequency zonal flows that play a dominant role in regulating toroidal drift wave turbulence [5]. GAM can also be spontaneously generated and can regulate the turbulence [6], particularly in the edge region where the GAM frequency $\omega_{\rm GAM}$ is typically smaller than the drift wave frequency and the linear damping rate γ is small because of the large q [7–9].

GAM linear properties [10–14] and excitations [15–19] have been extensively studied in theory and simulation. On the other hand, GAM nonlinear self-interactions have not attracted much attention due to the fact that GAM has a wavevector only in the radial direction, which precludes both conventional $E \times B$ and polarization nonlinearities. However, the second harmonic frequency of GAM ($2\omega_{\rm GAM}$) has recently been observed in the JFT-2M [20] and DIII-D [21] tokamaks, providing clear evidence of the nonlinear GAM interactions. The generation of the second (and higher) harmonic represents an energy sink for the primary GAM oscillation [17, 18, 22]. Thus the nonlinear interactions offer a possible GAM saturation mechanism in addition to the energy coupling back to the ambient turbulence [23] and the energy sink because of the linear Landau and collisional damping. Nonlinear self-interaction of GAM has recently been studied using fluid theory with conflicting results [24–26].

In this work, we use a gyrokinetic particle simulation and a nonlinear gyrokinetic theory to study the nonlinear GAM self-interactions. In the global gyrokinetic toroidal code (GTC) [5, 27, 28] simulations, the primary GAM is excited by an initial perturbation of the ion guiding centre density uniform on the flux surface [29]. GTC simulations of a small amplitude GAM recover the analytic linear dispersion relation. When the GAM amplitude increases to the experimentally relevant level, GTC simulations without the parallel nonlinearity find the

[a] Author to whom any correspondence should be addressed.

generation of the second harmonic ($\omega = 2\omega_{\rm GAM}$) quasimodes, which are dominated by a potential perturbation with $n = m = 0$ and a density perturbation with $n = 0, m = 1$. The generation rate of the second harmonic is proportional to the intensity of the primary GAM. The radial wavevector of the quasimode is twice that of the primary GAM. The poloidal structures of the density perturbation of the quasimodes are measured from simulations for comparisons with the gyrokinetic theory. All these simulation results are consistent with the expectation for a quadratic nonlinearity and agree well with the nonlinear gyrokinetic theory [30] in toroidal geometry when the parallel nonlinearity is also neglected. Specifically, the GTC simulation and the nonlinear gyrokinetic theory agree well on the amplitude and the mode structure of the second harmonic. The nonlinear gyrokinetic theory also shows that the quadratic nonlinearity comes from a nonlinear toroidal coupling due to the convection of the $n = 0, m = 1$ density perturbation by the $E \times B$ drift of the $n = m = 0$ potential perturbation. Therefore, this quadratic nonlinearity is induced by the compressibility of the $E \times B$ drift in the toroidal geometry with a geodesic curvature. This perpendicular convective nonlinearity is different from the conventional $E \times B$ nonlinearity or the polarization nonlinearity that drives a nonlinear toroidal coupling [31, 32].

However, more careful analysis of the nonlinear gyrokinetic theory for the GAM self-interaction finds that the perpendicular convective nonlinearity can be cancelled by the parallel nonlinearity in the long wavelength limit ($k_r\rho_{\rm i} \ll 1$, where k_r is the GAM radial wavelength and $\rho_{\rm i}$ is the ion gyroradius). Indeed, subsequent GTC simulation confirms that the generation of the second harmonic of the GAM is much weaker when the parallel nonlinearity is maintained in the simulation. Although the perpendicular convective nonlinearity cannot be cancelled by the parallel nonlinearity when $k_r\rho_{\rm i} \approx 1$, the short wavelength GAM itself is heavily damped by the high order resonance [10]. Therefore, our nonlinear gyrokinetic theory and GTC simulation conclude that the conventional GAM nonlinearity cannot efficiently generate the second harmonic of the long wavelength GAM. Other mechanisms, such as energetic particle nonlinearity, are required to explain recent experimental observations of the excitation of the GAM second harmonic [20, 21]. Furthermore, the parallel nonlinearity is neglected in most of gyrokinetic or fluid theory and simulation with the notable exception of [33–35] in which its influence on core ITG turbulence driven heat flux was shown to be negligibly small. On the other hand, our findings highlight the importance of the parallel nonlinearity in some applications such as the GAM self-interaction.

The paper is organized as follows. In section 2, GTC simulations of the GAM second harmonic are presented. In section 3, a nonlinear gyrokinetic theory is developed and compared with the GTC simulation results. Section 4 is the conclusion and discussion.

2. Gyrokinetic particle simulation

In our GTC simulations, the following D-IIID experiment parameters are used [36]: a major radius $R = 1.7$ m, an inverse aspect ratio $\epsilon = a/R = 0.35$, where a is the minor radius, a toroidal magnetic field $\boldsymbol{B}_0 = 2$ T and a temperature $T_{\rm e} = T_{\rm i} = 1$ keV on the flux surface of the GAM measurement. The radial wavevector is estimated to be $k_r\rho_{\rm i} = 0.1$, where $\rho_{\rm i} = v_{\rm i}/\Omega_{\rm i}$ is the ion Larmor radius and $v_{\rm i} = \sqrt{T_{\rm i}/m_{\rm i}}$, $\Omega_{\rm i} = eB_0/m_{\rm i}$ with $m_{\rm i}$ the ion mass. Electron response is set to be adiabatic for $n = 0, m \neq 0$ modes and homogeneous plasmas are used in our nonlinear GAM simulation. In the D-IIID experiment, the reversed shear is used with $q_{\rm min} = 3.5$ near $r = 0.5a$ where the GAM measurement was made [21]. Since our simulation is focused on the middle region of D-IIID, we use a simulation domain $\Delta r = [0.3a, 0.7a]$ and a constant $q = 3.5$ as the magnetic shear has no effect on the $n = 0$ GAM and zonal modes. We also note that since we focus on the nonlinear GAM interactions, the constant simulation profile can help us minimize the complexity because there is no GAM continuum damping or mode conversion to short wavelength kinetic modes in this situation.

2.1. Simulation without parallel nonlinearity

To study the linear GAM properties, we first simulate a small amplitude GAM by using an initial perturbed distribution for ion guiding centres: $\delta f_{00} = (\delta n_{00}/n_0)F_{\rm M}$, where $(\delta n_{00}/n_0)_{\rm max} = 10^{-6}$ and $F_{\rm M}$ is a uniform Maxwellian, $F_{\rm M} = n_0(1/2\pi v_{\rm i})^{3/2}\exp(-v^2/v_{\rm i}^2)$. Figure 1(*a*) is the time evolution of the electric field E_r with $n = m = 0$ and a numerical fitting result. The fitting function is defined as

$$E_r(t) = Ae^{{\rm i}(\omega t+\alpha)} \qquad \text{where } \omega = \omega_{\rm GAM} + {\rm i}\gamma, \tag{1}$$

where $\omega_{\rm GAM}$ and γ are GAM real frequency and damping rate, respectively [3]. The numerical fitting result is $(\omega_{\rm GAM}, \gamma) = (1.71, 0.0124)(v_{\rm i}/R)$. $\omega_{\rm GAM}$ corresponds well with the analytical solution with an error less than 1%, while γ is slightly larger than a prediction by the second order theory [10]. More accurate theory needs to include the higher order solution [11, 12] and nonlocal effects. Figure 1(*b*) is the frequency spectrum of E_r. The sharp peak at $\omega = \omega_{\rm GAM} = 1.71v_{\rm i}/R$ corresponds to the linear GAM frequency. The amplitude at $\omega = 0$ is small since the residual level of zonal flow is $E_r(\infty)/E_r(0) \approx 0.02$ according to the zonal flow theory [37].

Next, we study nonlinear GAM interactions by initializing a large amplitude GAM in GTC simulations. In the D-IIID experiment, the nonlinear generation of the second harmonic of GAM has been observed. The detected GAM density fluctuation near the mid-plane is around 1–2% and the extrapolated peak fluctuation is 10–15%. In our simulations, we use an initial perturbation of the ion guiding centre density $\delta n_{00}/n_0 = 0.01$. Other simulation parameters are kept the same as in the small amplitude simulation of figure 1(*a*). Note that there is no particle density perturbation of the $n = m = 0$ mode since electrons do not respond to this mode. The particle density perturbation, on the other hand, is the same as the gyro-averaged ion guiding centre density perturbation δn_{01} since electron is adiabatic to $m \neq 0$ modes. The density perturbation $\delta n_{01}/n_0$ is initially zero, but rises within a GAM oscillation period to a value of $\delta n_{01}/n_0 \approx 0.1$. This is a linear coupling due to the compressibility of the $E \times B$ drift of the $n = m = 0$ mode. The second harmonic with a characteristic frequency of $2\omega_{\rm GAM}$ is observed in this nonlinear regime as we can see from

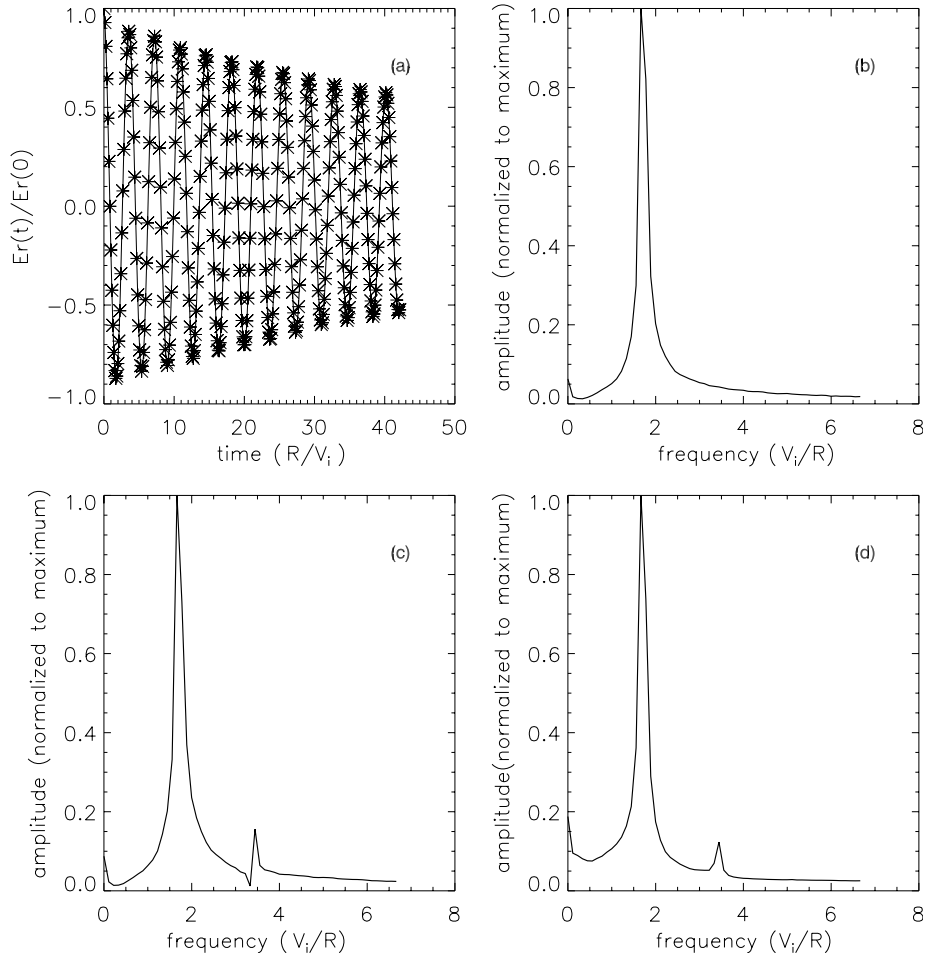

Figure 1. GTC simulations without parallel nonlinearity: (*a*) and (*b*) are the time evolution and frequency spectrum of E_r in a small amplitude simulation. In (*a*) the symbols are simulation data, the solid line is a numerical fitting. (*c*) and (*d*) are the frequency spectra of E_r and δn_0, respectively, in a large amplitude simulation.

figure 1(*c*). From the δn_0 spectrum (figure 1(*d*)), we find that both the second harmonic component and a zero-frequency density perturbation component are excited. This indicates that when GAM amplitude grows large sufficiently, a three-wave interaction process occurs: GAM couples with itself and produces two branches of daughter waves, i.e. a zero-frequency component and the second harmonic component. These results obey the frequency selection rules, i.e.

$$\omega_1 \pm \omega_2 = \omega_3, \qquad \text{where } \omega_1 = \omega_2 = \omega_{\rm GAM}, \quad \omega_3 = 0 \text{ or } 2\omega_{\rm GAM}, \tag{2}$$

$$k_1 + k_2 = k_3, \qquad \text{where } k_1 = k_2 = k_0, \quad k_3 = 2k_0. \tag{3}$$

This nonlinear coupling is a quadratic nonlinearity originated from the toroidal compressibility. Therefore, the wavevector must also follow the matching condition. Note that the nonlinearly generated modes of $\omega = 0$ and $\omega = 2\omega_{\rm GAM}$ are not normal modes and we only consider the $k_3 = 2k_0$ mode since the $k_3 = 0$ would result in an infinite radial wavelength.

An important signature of the quadratic nonlinearity is that the generation rate of the second harmonic is proportional to the intensity of the pump wave. This is confirmed in figure 2(*a*), which shows that the spectral ratio of the second harmonic to the primary GAM is linearly proportional to the amplitude of the primary GAM measured from a series of simulations with different initial GAM amplitudes. Here we use the magnitude of the frequency spectrum of radial electric field E_r in a time domain of $[0, 56.6R/v_{\rm i}]$ to represent the mode amplitude since the damping rate of the primary GAM and the growth rate of the second harmonic are much smaller than $\omega_{\rm GAM}$. To calculate the strength of the nonlinear coupling, we fit the data in figure 2(*a*) to a straight line of $E_r^{\rm II}/E_r^{\rm I} = AE_r^{\rm I}$, where $E_r^{\rm I}$ and $E_r^{\rm II}$ (in the unit of $v_{\rm i}B_0$) are radial electric fields of the primary and the second harmonic, respectively. Here, A is a dimensionless constant representing the nonlinear coupling strength. We find $A \approx 0.95$ from the GTC simulations, in reasonable agreement with a theoretical result of $A \approx 0.58$ from a nonlinear gyrokinetic theory presented in section 3.

In this nonlinear mode coupling process, the GAM damping rate is found to increase with the amplitude of the primary GAM E_r (figure 2(*b*)). When the amplitude of E_r is small, i.e. the nonlinear generation of the second harmonic is negligible, the damping rate is a constant equal to the linear Landau damping rate. On the other hand, when it exceeds a critical value, i.e. $E_r \approx 0.01(1/Bv_{\rm i})$, the damping rate is almost proportional to the amplitude of E_r. This further confirms the observation that the second harmonic generation rate is proportional to the intensity of the primary

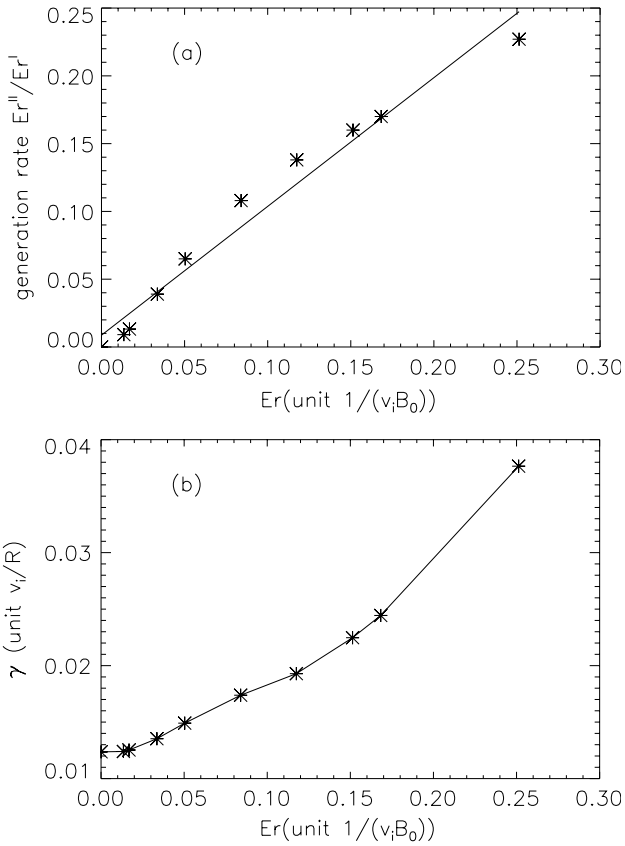

Figure 2. The second harmonic generation rate (a) and the primary GAM damping rate (b) versus amplitude of the primary GAM.

harmonic.

Finally, we construct the mode structures using time Fourier transform of the perturbed density on each grid in the poloidal plane:

$$\delta n_0(r,\theta,\omega) = \frac{1}{2\pi}\int \mathrm{d}t \mathrm{e}^{\mathrm{i}\omega t}\delta n_0(r,\theta,t). \qquad (4)$$

Then we pick up the complex values of each harmonic in the frequency spectrum for $\omega = 0, \omega_{\mathrm{GAM}}, 2\omega_{\mathrm{GAM}}$, respectively:

$$\delta n_0(r,\theta,0), \quad \delta n_0(r,\theta,\omega_{\mathrm{GAM}}), \quad \delta n_0(r,\theta,2\omega_{\mathrm{GAM}}). \qquad (5)$$

These mode structures are plotted in figure 3 on a poloidal plane as density contour plots for the zero-frequency harmonic, the primary harmonic and the second harmonic. The zero-frequency harmonic has only real part. From these figures we can see that the primary harmonic GAM is dominated by an $m = 1$ density perturbation with an up–down asymmetry, which corresponds well with the GAM theory [15]. The structures of the zero-frequency and the second harmonic components are also dominated by an $n = 0, m = 1$ density perturbation. Together with the $2\omega_{\mathrm{GAM}}$ peak in both the E_r with $n = m = 0$ and the density frequency spectrum (figures 1(c) and (d)), GTC simulations thus show that the second harmonic is dominated by an electrostatic potential with $n = 0, m = 0$ and a density perturbation with $n = 0, m = 1$ similar to the primary GAM. We can also see that the structures of the zero-frequency harmonic and the second harmonic have opposite phases as expected from the frequency matching condition of equations (2) and (3) . The structures of both the zero-frequency and the second harmonic have a poloidal angle shift from the primary harmonic. We find that the second harmonic poloidal angle shift depends on the inverse aspect ratio ϵ as shown in figure 4. As shown in section 3, the poloidal angle shift of the second harmonic is due to the competition between the nonlinear term $\delta\phi^{\mathrm{II}}_{\mathrm{nl}}$ and the linear term $\delta\phi^{\mathrm{II}}_{\mathrm{l}}$. The poloidal angle shift measured from GTC simulations agrees well with the gyrokinetic theory, as shown in figure 4.

Mode structures in figure 3 show that the radial scale length of the second harmonic is shorter than that of the primary mode. However, the radial wavevector matching condition is not clearly shown in these simulations due to the large simulation domain of $\Delta r = 0.4a$ (i.e. lack of radial symmetry in a realistic DIII-D equilibrium). By performing simulations of a thin annulus using artificial parameters of $\Delta r = 0.03a$ in a large torus, we can clearly see that the dominant radial wavevector of the second harmonic is $k^{\mathrm{II}}_r = 2k^{\mathrm{I}}_r$ as expected for the quadratic nonlinearity.

2.2. *Simulation with parallel nonlinearity*

In simulations presented in section 2.1, the parallel nonlinearity is neglected. Although in small GAM amplitude simulations, the removal of the parallel nonlinearity would cause no difference to the GAM evolution, the nonlinear interaction of GAM may be different when the GAM amplitude is large. Here we show that the parallel nonlinearity obviously suppresses the generation of the second harmonic in large amplitude GAM simulation, as predicted by the nonlinear gyrokinetic theory.

We use the same D-IIID experimental parameters to perform the simulation but keep the parallel nonlinearity. Figure 5(a) is the frequency spectrum of the perturbed density δn_0, which shows that the second harmonic is suppressed by the parallel nonlinearity compared with figure 1(d). However, the zero-frequency mode seems to have little changes. The suppression of the second harmonic by the parallel nonlinearity can also be derived from the nonlinear gyrokinetic equation with the parallel nonlinearity term, which shows that the parallel nonlinearity term cancels the perpendicular drift nonlinear term in the lowest order of $k_r\rho_{\mathrm{i}}$ (see section 3). Although the second harmonic is suppressed, the GAM damping rate is still enhanced probably due to the generation of the zero-frequency mode, but this damping rate is not as large as the result without parallel nonlinearity (figure 5(b)). Figure 6 is the mode structures of the zero-frequency mode and the second harmonic in the simulation with the parallel nonlinearity. We can see that the mode structure of the zero-frequency mode has little change when compared with figure 3(a). But the second harmonic mode becomes much weaker, and the imaginary part of the second harmonic seems to have no steady structure like figure 3(c).

3. Nonlinear gyrokinetic theory

In order to better understand the GAM nonlinear interactions, we use nonlinear gyrokinetic theory to compare with the

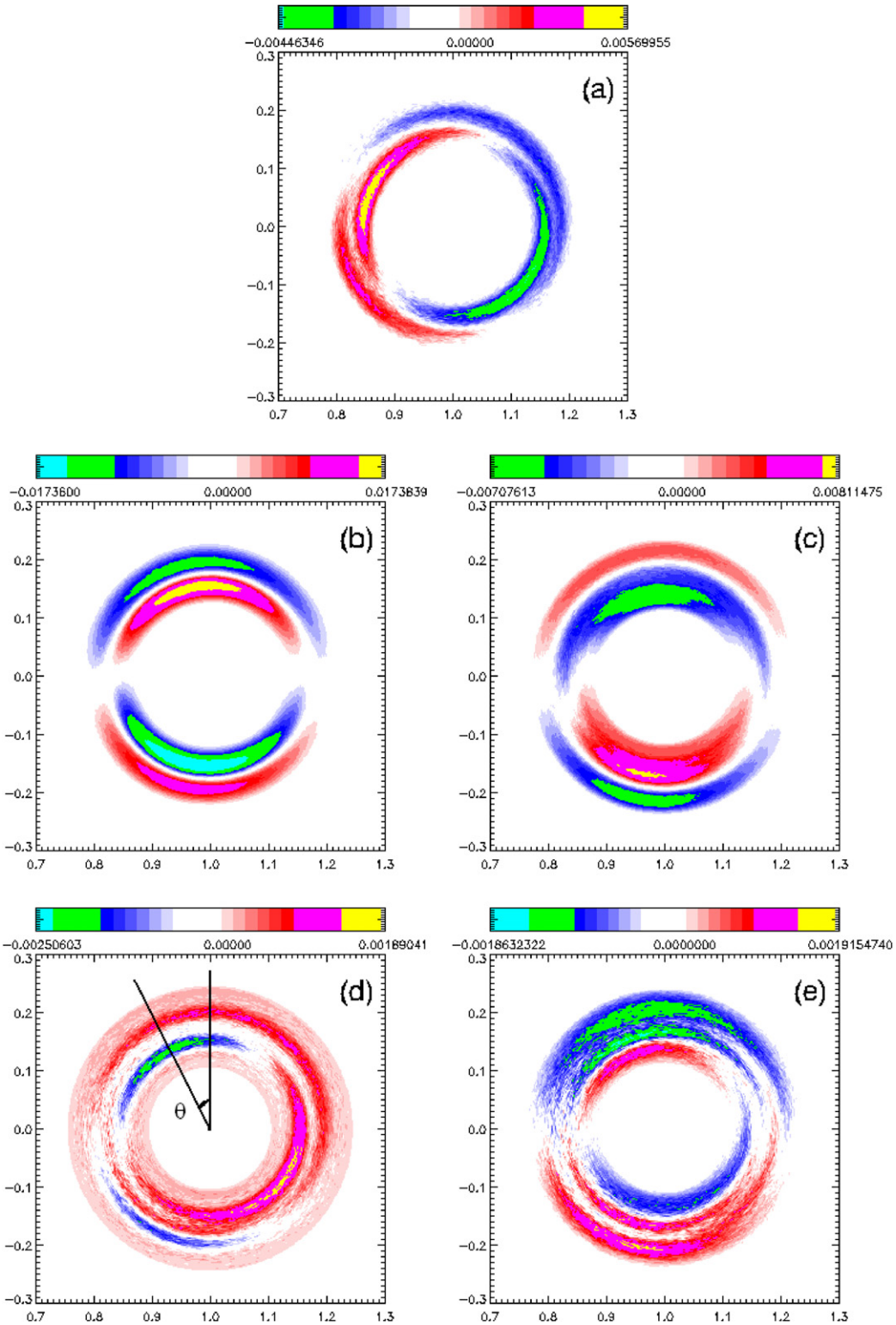

Figure 3. Density mode structures of the zero-frequency harmonic (top panels), the primary harmonic (middle panels) and the second harmonic (bottom panels). The left column is real components and the right column is imaginary components.

GTC simulations of the generation of the second harmonic. We consider a large aspect ratio axisymmetric tokamak with equilibrium magnetic field given by $\boldsymbol{B} = B_0(\boldsymbol{e}_\xi/(1+\epsilon\cos\theta)+(\epsilon/q)\boldsymbol{e}_\theta)$, where ξ and θ are, respectively, the toroidal and poloidal angles of the torus.

We use the nonlinear gyrokinetic equation, in its phase space-conserving form [38, 39],

$$\frac{\partial}{\partial t}(B_\parallel^* F) + \frac{\partial}{\partial \boldsymbol{X}}(B_\parallel^* \dot{\boldsymbol{X}} F) + \frac{\partial}{\partial W}(B_\parallel^* \dot{W} F) = 0, \qquad (6)$$

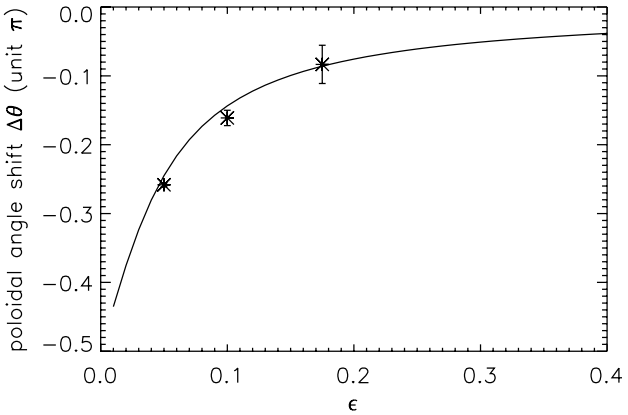

Figure 4. Dependence of the poloidal angle shift $\Delta\theta$ on the inverse aspect ratio ϵ. These simulations are done with a large torus and small simulation region $\Delta r = 0.03a$. The solid line is theory prediction, the dots are simulation results.

where $F = F(\boldsymbol{Z}, t)$, $\boldsymbol{Z} = (\boldsymbol{X}, W, \mu)$ is the five-dimensional gyrocentre phase space with $\boldsymbol{X}$, W and μ being the gyrocentre position, the parallel velocity and the magnetic moment, respectively. $B_\parallel^* = \hat{\boldsymbol{b}} \cdot \boldsymbol{B}^*$, $\hat{\boldsymbol{b}} = \boldsymbol{B}/B$, $\boldsymbol{B}^* = \boldsymbol{B} + (B/\Omega)\bar{\nabla} \times (W\hat{\boldsymbol{b}})$ and $\bar{\nabla} \equiv \partial/\partial \boldsymbol{X}$. We have, in equation (6), furthermore, that

$$\dot{\boldsymbol{X}} = \frac{\boldsymbol{B}}{\Omega B_\parallel^*} \times \bar{\nabla} H + \frac{\boldsymbol{B}^*}{B_\parallel^*} \frac{\partial}{\partial W} H, \tag{7}$$

$$\dot{W} = -\frac{\boldsymbol{B}^*}{B_\parallel^*} \cdot \bar{\nabla} H, \tag{8}$$

$$H = \mu B + W^2/2 + (e/m)\langle \delta\phi \rangle \equiv H_0 + \delta H. \tag{9}$$

Here $\delta\phi$ is the perturbed scalar potential, Ω is the gryofrequency, $\langle \cdots \rangle$ denotes average over the gyrophase angle while holding $\boldsymbol{Z}$ constant. For weakly nonlinear calculations, we keep only the linear perturbations δH in the Hamiltonian H. Here we note the gyrocentre phase-space conservation property:

$$0 = \nabla \cdot (B_\parallel^* \dot{\boldsymbol{X}}) + \frac{\partial}{\partial W}(B_\parallel^* \dot{W}), \tag{10}$$

which is exact to all orders in the gyrocentre analysis.

The nonlinear gyrokinetic equation (6), in the case of the second harmonic generation, can be rewritten as

$$\left(\frac{\partial}{\partial t} + \mathrm{i}\omega_\mathrm{d}\right) \delta F^\mathrm{II} + \delta \dot{\boldsymbol{X}}^\mathrm{I} \cdot \frac{\partial}{\partial \boldsymbol{X}} \delta F^\mathrm{I} + \delta \dot{W}^\mathrm{I} \frac{\partial}{\partial W} \delta F^\mathrm{I} = 0, \tag{11}$$

in which $\omega_\mathrm{d} = \hat{\omega}_\mathrm{d} \sin\theta = -k_r m_\mathrm{i}(v_\perp^2/2 + v_\parallel^2) \sin\theta/(eBR)$ is the magnetic drift associated with the geodesic curvature, the superscripts I and II represent the primary and the second harmonic, respectively. Here, we consider only the lowest order nonlinear effects, thus we ignore the $O(\omega_\mathrm{d}/\omega) \approx O(k_r \rho_\mathrm{i})$ term. For the electrostatic case, we have

$$\delta \dot{\boldsymbol{X}}^\mathrm{I} = \frac{1}{B} \hat{\boldsymbol{b}} \times \nabla \langle \delta\phi^\mathrm{I} \rangle, \tag{12}$$

$$\delta \dot{W}^\mathrm{I} = -\frac{e}{m} \hat{\boldsymbol{b}} \cdot \nabla \langle \delta\phi^\mathrm{I} \rangle - \frac{1}{B} \nabla \times (W\hat{\boldsymbol{b}}) \cdot \nabla \langle \delta\phi^\mathrm{I} \rangle. \tag{13}$$

We note that in equation (11), the second term is the usual perpendicular nonlinear convective term and the last term is the parallel nonlinear term. In the usual gyrokinetic ordering, the parallel nonlinear term is neglected compared with the perpendicular nonlinear convective term:

$$\left| \frac{\frac{e}{m} \hat{\boldsymbol{b}} \cdot \nabla \langle \delta\phi \rangle \frac{\partial}{\partial W} \delta F}{\frac{1}{B} \hat{\boldsymbol{b}} \times \nabla \langle \delta\phi \rangle \cdot \frac{\partial}{\partial X} \delta F} \right| \approx \frac{1}{k_r \rho_\mathrm{i} k_\theta R} \ll 1. \tag{14}$$

From the linear calculation [14], we have the linear responses of ions, to the lowest order given by

$$\delta F = -\frac{e}{T} F_\mathrm{M} \langle \delta\phi \rangle + \delta G \approx \frac{\hat{\omega}_\mathrm{d}}{\omega} \frac{e}{T_\mathrm{i}} F_\mathrm{M} \delta\phi_{00} \sin\theta, \tag{15}$$

where subscript 00 denotes the $n = 0$, $m = 0$ component. The perpendicular nonlinear convective term is given by

$$\delta F^\mathrm{II}_\mathrm{nl,R} = -\frac{e^2 k_r^\mathrm{I}}{m\Omega T_\mathrm{i} r} \frac{\hat{\omega}_\mathrm{d}}{\omega^\mathrm{I}\omega^\mathrm{II}} F_0 \cos\theta (\delta\phi_{00}^\mathrm{I})^2. \tag{16}$$

The electrons can be described by the adiabatic response. If we neglect the parallel nonlinearity term, the flux surface averaged quasi-neutrality condition for the second harmonic yields

$$\left(1 - \frac{\omega_\mathrm{GAM}^2(r)}{(\omega^\mathrm{II})^2}\right) \delta\phi_{00}^\mathrm{II} + \frac{e}{m\omega^\mathrm{I}\omega^\mathrm{II} R^2} \left(\frac{k_r^\mathrm{I}}{k_r^\mathrm{II}}\right)^2 (\delta\phi_{00}^\mathrm{I})^2 = 0. \tag{17}$$

Here, the first term is obtained from the linear GAM dispersion relation, while the second term is from the contribution of the perpendicular nonlinear convective term ($\delta F^\mathrm{II}_\mathrm{nl,R}$). Frequency and wavenumber matching conditions yield $\omega^\mathrm{II} = 2\omega^\mathrm{I}$, $k_r^\mathrm{II} = 2k_r^\mathrm{I}$ and $m = n = 0$ for the second harmonic as observed in GTC simulation. We note that the contribution of the flux surface averaged $\delta F^\mathrm{II}_\mathrm{nl,R}$ under quasi-neutrality condition comes from the toroidal coupling. The ratio between the amplitude of the second and primary harmonic of GAM is thus, given by

$$\left| \frac{\delta E_r^\mathrm{II}}{\delta E_r^\mathrm{I}} \right| = \frac{1}{6S} \frac{e}{T_\mathrm{i}} \delta\phi_{00}^\mathrm{I} \qquad \text{where } S = \left(\frac{R\omega_\mathrm{GAM}}{v_\mathrm{i}}\right). \tag{18}$$

In GTC simulations, this formula can be normalized as

$$\left| \frac{\delta E_r^\mathrm{II}}{\delta E_r^\mathrm{I}} \right| = A \frac{\delta E_r^\mathrm{I}}{B v_\mathrm{i}}, \qquad \text{where } A = \frac{1}{6S k_r^\mathrm{I} \rho_\mathrm{i}}. \tag{19}$$

In our simulations with $k_r^\mathrm{I}\rho_\mathrm{i} = 0.1$ and $S = 2.9$, we get $A = 0.58$ as mentioned in section 2.1. This indicates that the second harmonic generation rate is proportional to the intensity of the primary harmonic, which is consistent with GTC simulation results. We emphasize that there is no threshold for the second harmonic generation, since this corresponds to a driven excitation rather than a spontaneous excitation.

In the $k_r \rho_\mathrm{i} \ll 1$ limit, the corresponding density perturbation is dominated by the $m = 1$ poloidal component:

$$\delta n_0 = (a\cos\theta + b\sin\theta) \frac{e}{T_\mathrm{i}} (\delta\phi_{00}^\mathrm{I})^2 = \sin(\theta + \Delta\theta) \frac{e}{T_\mathrm{i}} (\delta\phi_{00}^\mathrm{I})^2. \tag{20}$$

Here, $a = -k_r \omega_{\mathrm{d}t}/(2rB\omega^2)$ and $b = e\omega_{\mathrm{d}t}(1+\tau)/(3S\omega T_\mathrm{i})$ enter, respectively, via $\delta F^\mathrm{II}_\mathrm{nl,R}$ and $\delta F^\mathrm{II}_\mathrm{l}$. Meanwhile, $w_{\mathrm{d}t} = kr\rho_\mathrm{i} v_\mathrm{i}/R_0$, $\Delta\theta$ is the poloidal angle shift of the second

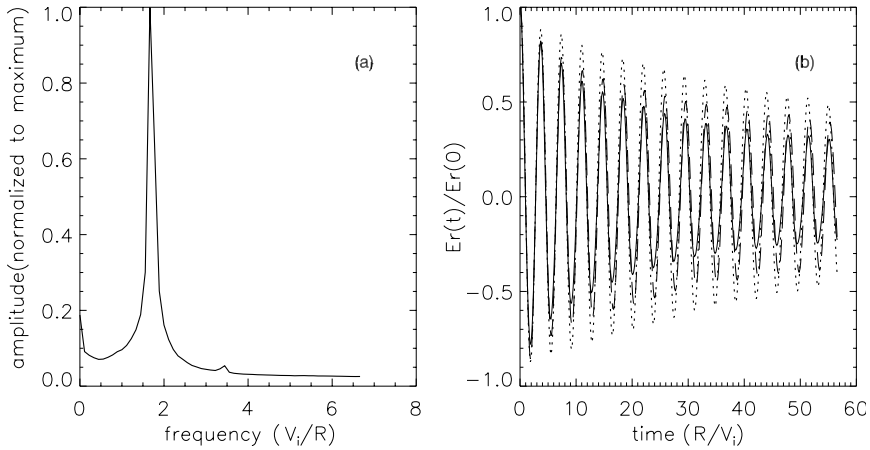

Figure 5. Frequency spectrum of δn_0 (a) from large amplitude simulation with parallel nonlinearity and time evolution of E_r (b). In (b), the dotted line is the small amplitude simulation results, the dashed line and the solid line are the large amplitude simulation with and without parallel nonlinearity results, respectively.

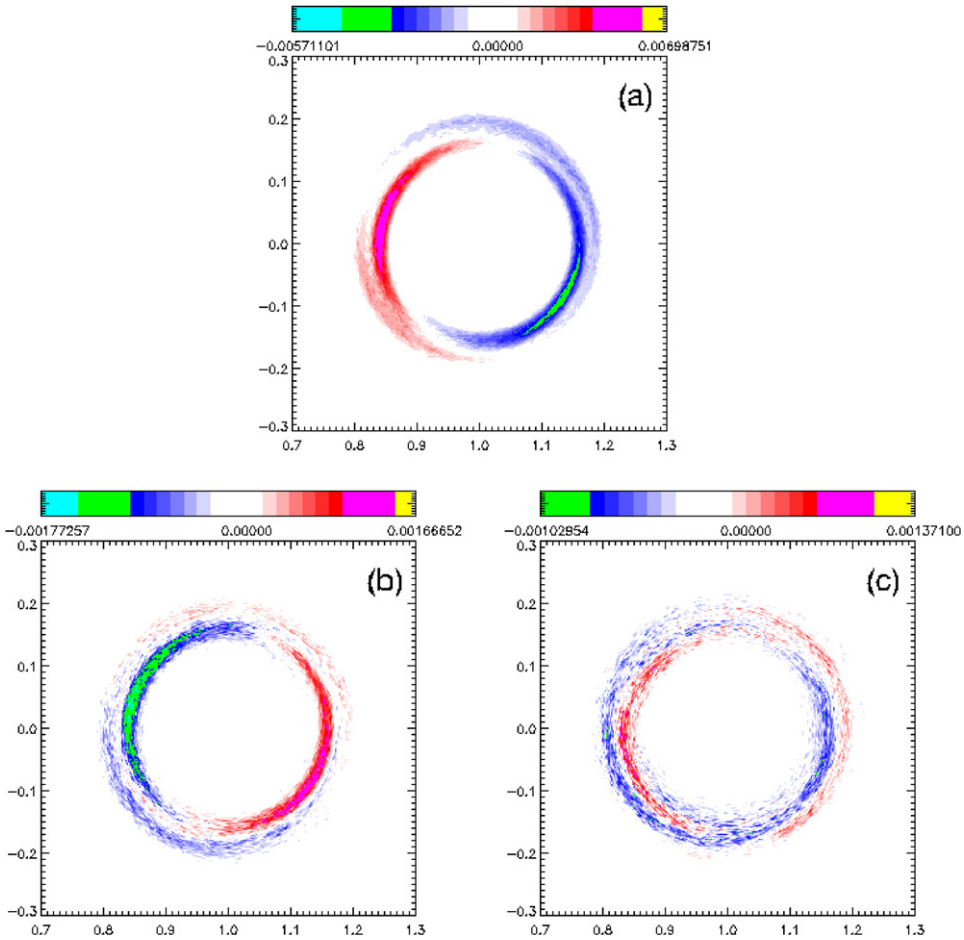

Figure 6. Density mode structures of the zero-frequency harmonic (top panel) and the second harmonic (bottom panels). The left column is real components and the right column is imaginary components.

harmonic from the primary harmonic (figure 3(d)), and is given by

$$\Delta\theta = \tan^{-1}(a/b) = \tan^{-1}\left(\frac{-3\sqrt{S}k_r\rho_{\rm i}}{4(1+\tau)\epsilon}\right), \qquad (21)$$

which has a dependence on both ϵ and $k_r\rho_{\rm i}$. Figure 4 shows that GTC simulation results agree well with that predicted by equation (21). We note that equation (21) is valid in the large aspect ratio limit, i.e. $\epsilon \ll 1$.

As we pointed out previously, the contribution of the flux surface averaged perpendicular nonlinear convective term comes from the toroidal coupling, which is smaller than the optimal ordering of the perpendicular nonlinear convective term by a factor of r/R. Thus, it is comparable to the parallel

nonlinear term. So here we need to include the contribution of the parallel nonlinear term, which is given by

$$\delta F^{\rm II}_{\rm nl,P} = \frac{1}{{\rm i}\omega^{\rm II}} \delta \dot{W}^{\rm I} \frac{\partial}{B\partial W}(B\delta F^{\rm I}). \tag{22}$$

Integrating by parts, and employing the phase-space conserving property (equation (10)), we get

$$\delta F^{\rm II}_{\rm nl,P} = \frac{1}{{\rm i}\omega^{\rm II}} \left[\frac{\partial}{\partial W}(\delta F^{\rm I} \delta \dot{W}^{\rm I}) + \frac{\delta F^{\rm I}}{B} \nabla \langle \delta \phi^{\rm I} \rangle \cdot \nabla \times \hat{\boldsymbol{b}} \right]. \tag{23}$$

The first term is a full derivative, and will vanish in the velocity space integration. The second term, gives

$$\delta F^{\rm II}_{\rm nl,P} = \frac{e^2 k_r^{\rm I}}{m\Omega T_{\rm i} R} \frac{\hat{\omega}_{\rm d}}{\omega^{\rm I}\omega^{\rm II}} F_0 \sin^2\theta (\delta\phi^{\rm I}_{00})^2. \tag{24}$$

After doing surface averaging to $\delta F^{\rm II}_{\rm nl,R}$ and $\delta F^{\rm II}_{\rm nl,P}$, we find that these two terms will cancel exactly with each other, i.e.

$$\overline{\delta F^{\rm II}_{\rm nl,P}} = -\overline{\delta F^{\rm II}_{\rm nl,R}} = \frac{e^2 k_r^{\rm I}}{2m\Omega_{\rm i} T_{\rm i} R} \frac{\hat{\omega}_{\rm d}}{\omega^{\rm I}\omega^{\rm II}} F_0 (\delta\phi^{\rm I}_{00})^2. \tag{25}$$

Here $\overline{(\ldots)}$ means surface average. So the nonlinear harmonic generation of GAM is of a higher order in the $O(\omega_{\rm d}/\omega) \approx O(k_r\rho_{\rm i})$ effect than the parallel nonlinearity term, and is thus, ignorable. This result can be directly seen from our simulation with the parallel nonlinearity in section 2.2, which shows that the second harmonic is suppressed by the parallel nonlinearity.

4. Conclusion and discussion

Gyrokinetic theory and simulation find that nonlinear self-interactions of the GAM in toroidal plasmas cannot efficiently generate the second harmonic due to a cancellation between the perpendicular convective nonlinearity and the parallel nonlinearity for the long wavelength GAM. Other mechanisms are required to explain recent experimental observations of the excitation of the GAM second harmonic. Our findings also raise the issue of the validity of the nonlinear GAM theory proposed to explain the generation of the GAM second harmonic as observed in tokamak experiments. Our finding indicates that the toroidal geometry, and in some situations the parallel nonlinearity, is important for the correct description of the nonlinear behaviours of the fusion plasmas.

Acknowledgments

One of the authors (H.S. Zhang) acknowledges useful discussions with I. Holod, Y. Xiao, W.L. Zhang and J.Q. Li. This work was supported by the US Department of Energy (DOE) SciDAC GSEP and GPS centers, DOE and NSF grants at UCI, and NSFC, Grant Nos 40731056, 10778613, and the National Basic Research Programme of China, Grant Nos 2008CB787103 and 2008CB717806.

References

[1] Winsor N., Johnson J.L. and Dawson J.J. 1968 *Phys. Fluids* **11** 2448
[2] Levedev V.B. *et al* 1996 *Phys. Plasmas* **3** 3023
[3] Novakovskii S.V. *et al* 1997 *Phys. Plasmas* **4** 4272
[4] Fujisawa A. 2009 *Nucl. Fusion* **49** 013001
[5] Lin Z. *et al* 1998 *Science* **281** 1835
[6] Hallatschek K. and Biskamp D. 2001 *Phys. Rev. Lett.* **86** 1223
[7] Hahm T.S. *et al* 2000 *Plasma Phys. Control. Fusion* **42** A205
[8] Zhao K.J. *et al* 2006 *Phys. Rev. Lett.* **96** 255004
[9] Lan T. *et al* 2008 *Phys. Plasmas* **15** 056105
[10] Sugama H. and Watanabe T.H. 2006 *J. Plasma Phys.* **72** 825
[11] Gao Z. *et al* 2008 *Phys. Plasmas* **15** 072511
[12] Xu X.Q. *et al* 2008 *Phys. Rev. Lett.* **100** 215001
[13] Sasaki M. *et al* 2008 *Contrib. Plasma Phys.* **48** 68
[14] Qiu Z., Chen L. and Zonca F. 2009 *Plasma Phys. Control. Fusion* **51** 012001
[15] Itoh K., Hallatschek K. and Itoh S.I. 2005 *Plasma Phys. Control. Fusion* **47** 451
[16] Miki K. *et al* 2007 *Phys. Rev. Lett.* **99** 145003
[17] Chakrabarti N. *et al* 2007 *Phys. Plasmas* **14** 052308
[18] Zonca F. and Chen L. 2008 *Europhys. Lett.* **83** 35001
[19] Xiao Y. and Lin Z. 2009 *Phys. Rev. Lett.* **103** 085004
[20] Nagashima Y. *et al* 2007 *Plasma Phys. Control. Fusion* **49** 1611
[21] Nazikian R. 2008 private communication, Princeton Plasma Physics Laboratory
[22] Fu G.Y. 2008 *Phys. Rev. Lett.* **101** 185002
[23] Scott B.D. 2005 *New J. Phys.* **7** 92
[24] Sasaki M. *et al* 2009 *Phys. Plasmas* **16** 022306
[25] Sasaki M. *et al* 2009 *Plasma Phys. Control. Fusion* **51** 085002
[26] Mikhailovskii A.B. *et al* 2009 *Plasma Phys. Control. Fusion* **51** 075010
[27] Holod I. and Lin Z. 2007 *Phys. Plasmas* **14** 032306
[28] Zhang W.L., Lin Z. and Chen L. 2008 *Phys. Rev. Lett.* **101** 095001
[29] Lin Z. *et al* 2000 *Phys. Plasmas* **7** 1857
[30] Frieman E.A. and Chen L. 1982 *Phys. Fluids* **25** 502
[31] Lin Z., Chen L. and Zonca F. 2005 *Phys. Plasmas* **12** 056125
[32] Chen L., Zonca F. and Lin Z. 2005 *Plasma Phys. Control. Fusion* **47** B71
[33] Candy J. *et al* 2006 *Phys. Plasmas* **13** 074501
[34] Idomura Y. *et al* 2007 *J. Comput. Phys.* **226** 244
[35] Jolliet S. *et al* 2009 *Phy. Plasmas* **16** 072309
[36] Nazikian R. *et al* 2008 *Phys. Rev. Lett.* **101** 185001
[37] Rosenbluth M.N. and Hinton F.L. 1998 *Phys. Rev. Lett.* **80** 724
[38] Brizard A.J. 1995 *Phys. Plasmas* **2** 459
[39] Hahm T.J. 1988 *Phys. Fluids* **31** 2670